White Rose Research Online
eprints@whiterose.ac.uk
https://eprints.whiterose.ac.uk
Universities of Leeds, Sheffield and York

Deposited via The University of Sheffield.

White Rose Research Online URL for this paper:
https://eprints.whiterose.ac.uk/id/eprint/238161/

Version: Accepted Version

Article:

Nowak, P.R., Waddoups, R., Gajewski, T. et al. (2026) Fragmentation analysis for underwater ordnance disposal. International Journal of Protective Structures. ISSN: 2041-4196

https://doi.org/10.1177/20414196261421961

© 2026 The Authors. Except as otherwise noted, this author-accepted version of a journal article published in International Journal of Protective Structures is made available via the University of Sheffield Research Publications and Copyright Policy under the terms of the Creative Commons Attribution 4.0 International License (CC-BY 4.0), which permits unrestricted use, distribution and reproduction in any medium, provided the original work is properly cited. To view a copy of this licence, visit http://creativecommons.org/licenses/by/4.0/

Reuse
This article is distributed under the terms of the Creative Commons Attribution (CC BY) licence. This licence allows you to distribute, remix, tweak, and build upon the work, even commercially, as long as you credit the authors for the original work. More information and the full terms of the licence here: https://creativecommons.org/licenses/

Takedown
If you consider content in White Rose Research Online to be in breach of UK law, please notify us by emailing eprints@whiterose.ac.uk including the URL of the record and the reason for the withdrawal request.

UNIVERSITY OF LEEDS
University of Sheffield
UNIVERSITY of York

Fragmentation Analysis for Underwater Ordnance Disposal

Piotr Nowak[1], Ross Waddoups[2,4], Tomasz Gajewski[1], Dain Farrimond[2,4], Tommy Lodge[2,4], Genevieve Langdon[2], Andy Tyas[2,4], Piotr Sielicki[1], Elliot Tam[3], Mark Whittaker[3]

piotr.nowak@doctorate.put.poznan.pl – Poznan University of Technology, pl. M. Sklodowskiej-Curie 5, 60-965 Poznan, Poland

1 Poznan University of Technology, Poznań 60-965, Poland

2 University of Sheffield, Sheffield S13JD, UK.

3 Defence Science and Technology Laboratory, Salisbury SP4 0JQ, UK.

4 Blastech Ltd., Sheffield S14DP, UK.

piotr.nowak@doctorate.put.poznan.pl, rwaddoups1@sheffield.ac.uk, tomasz.gajewski@put.poznan.pl, d.farrimond@sheffield.ac.uk, t.j.lodge@sheffield.ac.uk, genevieve.langdon@sheffield.ac.uk, a.tyas@sheffield.ac.uk, piotr.sielicki@put.poznan.pl, etam@mail.dstl.gov.uk, mjwhittaker@dstl.gov.uk

Keywords: unexploded, ordnance, disposal, underwater, explosion, blast, fragments

Abstract

Explosive weapons may cause damage through both blast loading and fragmentation of their casings. Although air-detonated ordnance has been extensively studied, fragmentation hazards from underwater munitions remain underexplored, and therefore no standardised procedure exists to calculate safe standoff distances as a function of depth and charge mass in naval environments. This significantly hampers the safety planning process for underwater explosives ordnance disposal activities. Building on prior laboratory investigations of underwater fragmentation, this study extends the analysis toward full-scale applicability by estimating maximum fragmentation ranges and applying injury-criteria models to assess associated hazard limits. A series of well-controlled small-scale experiments compared cased explosive charges detonated in air and at varying submersion depths. Three casing configurations were tested to quantify the influence of depth and casing configuration type on fragment generation, in-flight behaviour, and size–velocity distributions. High-speed videography and in-situ witness panels were utilised to track fragmentation post-detonation and estimate velocities during flight and after impact. An in-house analysis code with optical and panel data was developed to compute fragment trajectories, maximum ranges, and soft-tissue penetration probabilities using established injury thresholds. Results indicate a pronounced reduction in fragment count, velocity and launch angle with increasing submersion depth, producing substantially shorter predicted penetration distances for all tested submerged charges. This paper outlines a practical methodology for scaling experimental observations toward larger charge masses and discusses implications for risk assessment and mitigation during underwater munitions clearance operations.

1. Introduction

Explosive ordnance, intact or during disposal, poses a significant threat to human life, environment, and any surrounding infrastructure. During the detonation of cased munitions, the rapid release of energy from the explosive charge transfers momentum to the casing material, resulting in the formation of high-velocity projectiles, usually of irregular mass and geometry governed by explosive composition, casing geometry and material properties (Zecevic et al., 2008). The hazard level associated with such fragmentation is governed by the probability of interaction, the kinetic energy of the fragments at the point of impact and the shape/sharpness of fragments (UNODA, 2021; Zaker, 1975). Any resultant fragments can exhibit wide ranges of velocities, trajectories and dimensions, creating additional hazards beyond the primary blast wave, and blunt trauma, which is the key safety determinant for underwater detonations.

Explosive ordnance disposal (EOD) operations are often unplanned and time-critical activities in which minimising the risk to personnel and the environment is the primary concern (Department of the Army, 2013a). Danger areas are typically estimated using the total explosive mass (TNT equivalence), with further safety factors applied – frequently in a subjective manner (UNODA, 2021). Incorporating additional information about the type and condition of the ordnance, its location, and its proximity to surrounding structures can substantially improve the accuracy of hazard assessments and help rationalise the selection of countermeasures (GICHD, 2017; 2022).

For cased explosives detonated in air, the blast and fragmentation parameters of most service munitions are well documented through manufacturer data (Australian Munitions, 2016), military procedures (Department of the Army, 1990), explosive safety standards (UNODA, 2021), and supplemented with scientific research (Absil et al., 1996). Numerous national and international publications (Zaker, 1975; Solomos et al., 2020) provide empirical correlations and simplified mathematical relationships for predicting fragment dispersion and impact energy in open-air detonations. These data sets are routinely applied during land-based EOD operations to determine safe working distances for personnel and to protect critical infrastructure (United Nations, 2021a; Department of the Army, 2011). Land-based unexploded ordnance (UXO), follow a defined safety protocol in which the minimum safe distance is either calculated or determined using established charts, tables, or risk assessment tools (Department of the Army, 1973; United Nations, 2013) to protect the public.

In contrast, the fragmentation hazards associated with underwater detonations remain poorly understood and seldom considered differently to air blasts. Current naval and humanitarian clearance operations often rely on qualitative judgment and operational experience rather than formal analytical procedures (GICHD, 2015), which may be different between EOD teams. This approach may be acceptable for deep-water operations, where fragments rapidly lose momentum due to hydrodynamic drag; however, it becomes inadequate in shallow coastal environments, where even limited fragment ranges may endanger divers, vessels and crew, or critical infrastructure. Because many underwater munitions lie at shallow depths—particularly those located near ports, harbours, and coastal installations (Nowak et al., 2021)—a more rigorous understanding of underwater fragmentation is essential for reliable hazard assessment and, consequently, to ensure that resources for protective measures are used effectively.

Underwater disposal imposes significant physiological and cognitive demands on personnel, while subjecting equipment to persistent mechanical, chemical, and hydrostatic stresses, and becomes even more complex for deep or partially buried UXO due to poor accessibility and the difficulty of extraction procedures (GICHD, 2015; HELCOM, 2024). Figure 1 illustrates a representative shallow-water scenario involving a sunken aerial munition (MK-82) requiring safe disposal. The illustration highlights two common resting positions of underwater ordnance: 1) lying flat on the seabed; and 2) partially embedded, with the nose buried and the body inclined. When the ordnance lies flat (in position 1), the centre of mass of the munition is located deeper below the water-air free surface than when the same body is tilted or nose-embedded (in position 2); consequently, the height of the water column above the explosive charge is greater for the flat-lying UXO. This varying water column height above a charge strongly influences formation and the likelihood of fragments breaching the free surface.

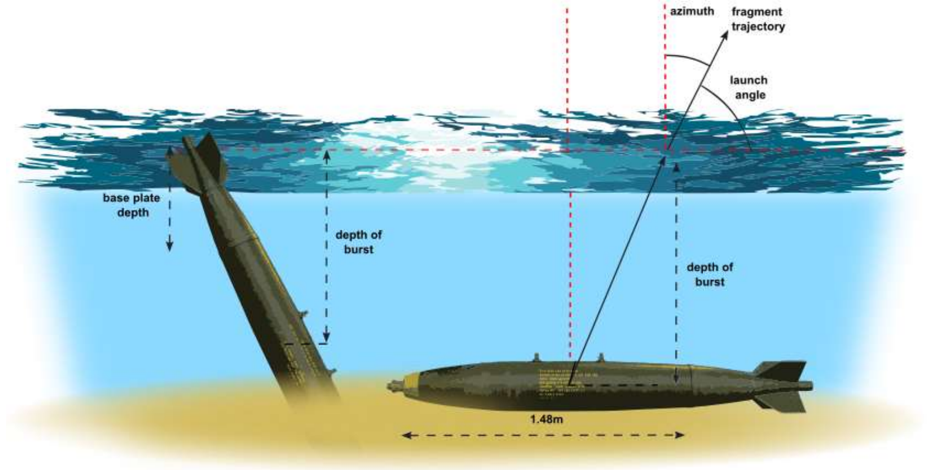

Figure 1. MK82 bomb in two positions at the bottom: nose buried and lying flat.

A recent real-world example underlines the operational importance of UXO orientation effects. In 2020, an earthquake bomb containing 2,400 kg of high explosive was discovered in a shallow waterway in Poland at a depth of approximately 12 m, posing an immediate hazard to marine traffic (Nowak et al., 2021). Under favourable conditions, such UXO would be lifted and towed to a designated disposal area (United Nations, 2021b); however, towing munitions increases exposure times and can reduce the effective water column above the charge, elevating the likelihood of fragment propagation and shrapnel injuries to personnel. Towing procedures increase the potential of accidental detonation of discovered unknown condition munitions through movement. In the absence of standardised towing-distance procedures, practitioners commonly use airburst fragmentation ranges as conservative references (Departments of the Army et al., 1990; Department of the Army, 2011); a practice that tends to overestimate the hazard zone. In real-life situations, it is often difficult to assess the effect of depth on the number of fragments and the maximum throw distance.

Existing munition casings produce fragments that vary widely in size, mass and shape, several authors have adopted idealised surrogate fragments to reduce variability and facilitate quantitative analysis. Qi et al. (2020) investigated the flight characteristics and momentum transfer of a blast-driven steel ball bearing embedded in a cylindrical charge, combining experiments and numerical modelling for air detonations. The use of such idealised projectiles permits clearer interpretation of velocity, trajectory and impact-energy data and supports the development of transferable predictive relationships.

A review of experimental and conceptual studies show that water-based mitigation concepts have been investigated, but few works translate these findings into prescriptive operational guidance for munitions disposal. Water is known to attenuate thermal radiation, air blast and fragment travel and is routinely used as a deceleration medium in fragmentation experiments (Zhao et al., 2020). For example, Schunck & Eckenfels (2021, 2024) evaluated water curtains positioned in front of perforated plates to reduce overpressure and impulse, while Gebekken (2019) examined the combined use of ring meshes and water curtains to attenuate shock-wave effects. Although these studies demonstrate measurable reductions in loading when water is employed as a barrier medium, they do not provide scalable decision criteria applicable to underwater UXO handling or the selection of safe towing distances.

Some experimental investigations indicate that fragments propelled into the air by underwater detonations may present lethal threats at considerable ranges, but the availability of any accompanying data sets is limited. Swisdak and Montanaro (1992) proposed a method to estimate maximum fragment range as a function of scaled explosion depth based on shallow-water tests of the MK-82 bomb, reporting fragment masses, velocities and travel distances. This work is often cited for its practical relevance to real-world events; however, its conclusions are derived from a relatively small number of trials, which limits both the statistical robustness of the results and the generalisability of the empirical scaling relations. Lee and Rude (2006) investigated the fragmentation behaviour of 143 g C4 charges at a depth of 0.45 m, analysing dispersion from a heavy steel casing. The study considered a charge-to-weight ratio of only about 7%, which is far lower than that typically found in military ordnance (~50% (Nowak et al., 2021)). Real systems contain proportionally much larger explosive fills and comparatively lighter casings, the study's findings should be applied with caution when extrapolating to conventional munitions.

Collectively, these works demonstrate the potential of water as a mitigating medium but reveal an important gap: experimental and conceptual results have not yet been assembled into operationally useful, scalable guidance for underwater UXO clearance. This study therefore aims to quantify how depth, casing type and munition position influence the fragment generation and maximum range.

Given the high cost and inherent risks of full-scale trials, the present work adopts a laboratory-scale methodology using small charges with the primary objective of this article being to translate these findings into guidelines for more robust practicable hazard estimation for clearance operations and compare directly to large-scale real-world events. The data recorded from well controlled small-scale trials are also essential for validating modelling methods which can be scaled accordingly to represent larger events to provide additional guidance with confidence.

The positive effectiveness of reduced-scale facilities for blast characterisation has been demonstrated previously in free-air studies (Farrimond et al., 2023) with similar control measures and techniques being implemented for research on underwater fragmentation dynamics for submerged charges was developed (Nowak et al, 2024a). This study advances the use of scaling from small-scale laboratory underwater explosions to full-scale real-world scenarios; to estimate the maximum fragmentation range from underwater explosive events and thus applying injury-criteria models to quantify risk to personnel and this establish empirically validated guidelines for full scale naval ordinance events.

2. Test Methods

This article presents an advanced analysis of 30 small-scale detonations previously reported by Nowak et al. (2024a). These tests were conducted within a cylindrical steel water tank (see Figure 2) at the University of Sheffield Blast and Impact Laboratory (UK) which was filled to various levels as per each test requirement. Detonated in these trials was a simplified, end-detonated cylindrical charge containing 46.5 ± 0.5 g PE10 which was then suspended within the tank and/or water column accordingly. A full, open-access description of the facility, setup, and procedures - including charge suspension, water-depth settings, and calibration - has been published in the article and is not repeated here; only a concise abstract is provided for completeness.

Three different casing configurations were examined to evaluate fragmentation phenomena: a machined solid-steel casing representative of a reduced-scale munition body (Figure 3a) and two sizes of spherical steel ball bearings (1.7mm and 2.6mm diameter) retained in 3D-printed jackets as constant-mass surrogate fragments (Figure 3b–c).

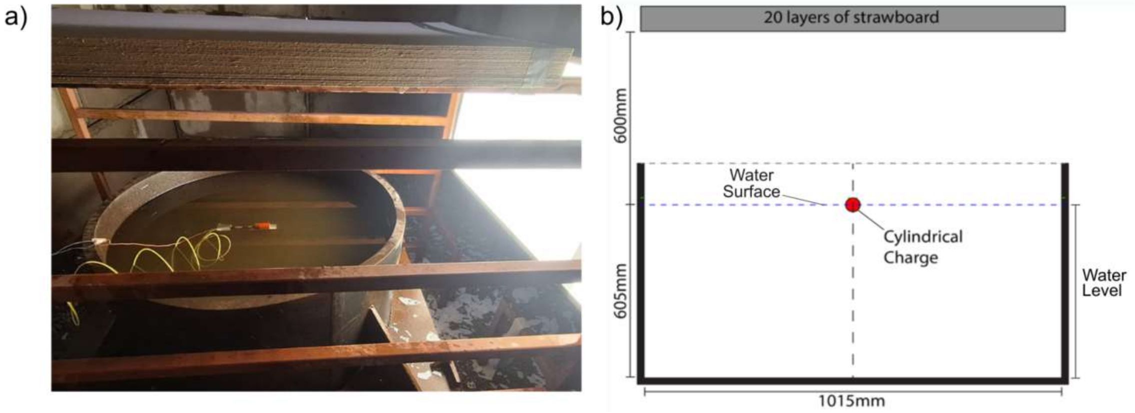

Figure 2. Experimental setup showing the steel water tank partially filled to the target depth (a) and a schematic of charge placement (b).

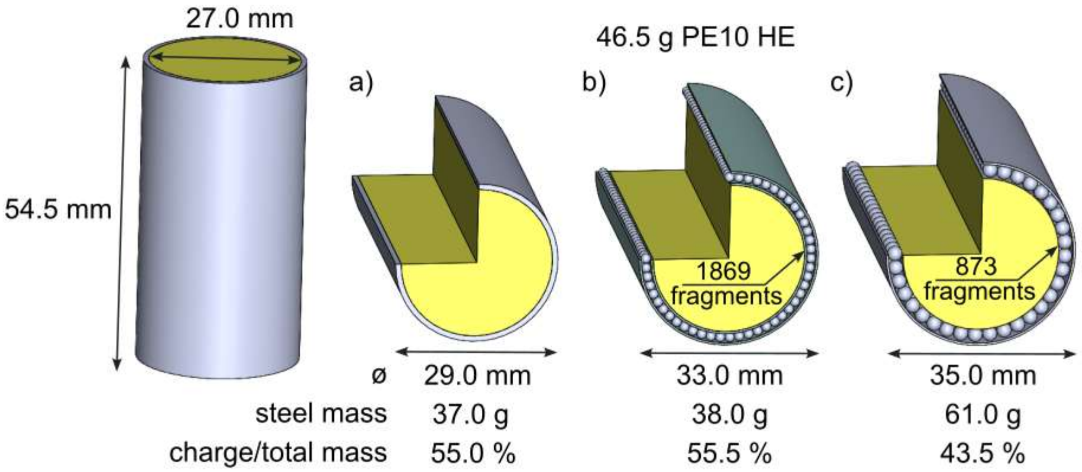

Figure 3. Test casings: (a) solid steel body and (b–c) small and large steel spheres in 3D-printed jackets.

For the steel ball bearing trials, two surrogate-fragment configurations were used: 1.7 mm and 2.6 mm ball bearings (total steel mass ~37 g and ~61 g, respectively), retained within 3D-printed jackets to produce average fragment counts of ~1,869 and ~873. The resulting charge-to-total-mass ratios (~55% and ~43%) are representative of common large-calibre ordnance (e.g., aerial bombs, naval mines; Nowak et al., 2021).

30 trials in total were performed exploring the effects on underwater fragmentation phenomena from varying casing types and water levels with full details and the complete dataset are available in Appendix A. The selected burst depths were determined to align with historical research related to ordnance to investigate the fragmentation scalability of underwater cased charges. Figure 4 presents a comparison between the 46.5 g PE10 tests conducted at depths of 60 mm and 110 mm with the heavily referenced Swisdak and Montanaro (1992) MK82 bomb trials, both presented in scaled depth. A significant conclusion from this work was that at a scaled depth of 1.47 m/kg$^{1/3}$ (4 m), fragmentation from the aerial bomb casing is considered negligible and will be explored further through well-controlled small scale trials.

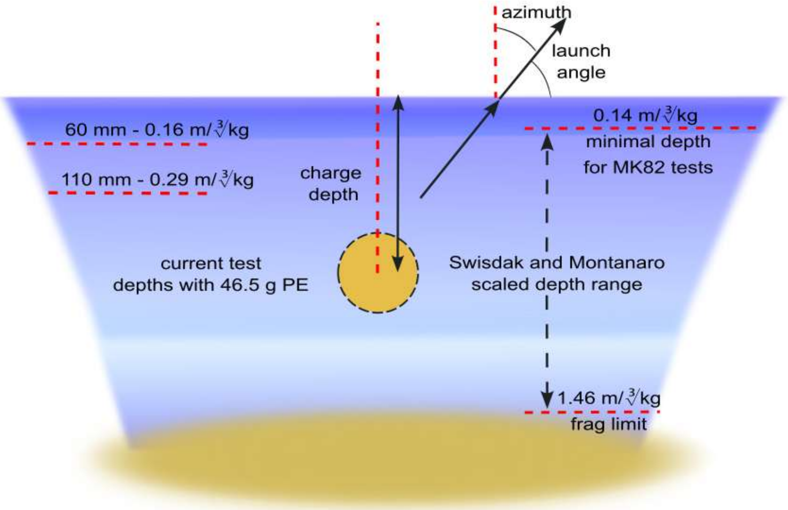

Figure 4. The scheme illustrating 46.5 g PE10 charge at 60 mm and 110 mm depth vs Swisdak and Montanaro (1992) scaled depth ranges.

For reference, four air tests (Setup A)—two with machined casings and two with 1.7 mm ball bearings—were conducted to characterise fragmentation without hydrodynamic effects. The remaining 26 tests examined the influence of water depth on fragment velocity and distribution at four relative charge positions: half-submerged, charge top at the surface, and charge-centre depths of 60 mm and 110 mm.

To infer fragment velocities from impact, a multi-layer strawboard witness panel (20 layers, 1500 × 750 × 3.7 mm; long centreline parallel to the cylinder axis) was suspended above the free water-air surface at a constant 600 mm radial offset from the charge centre to capture any resulting fragments (Figure 2). After each test, the witness panels were inspected for perforations and embedded fragments; these were marked with black ink to aid optical identification. Each strawboard panel was then photographed, and the images digitised and analysed with a house-built MATLAB script to determine per-layer penetration counts. Figure 5 illustrates the digitisation workflow.

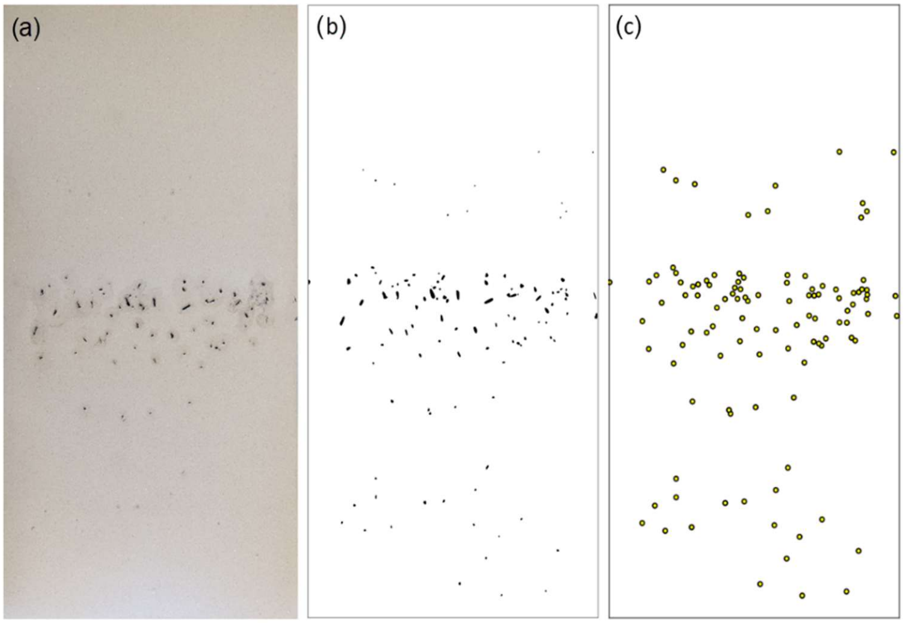

Figure 5. Fragmentation pattern for a machined steel casing detonated just below the surface: (a) original photography, (b) post-processed vector image and (c) centroids of fragment footprints.

Alongside the witness panel employed for fragment capture, the trials were recorded by one of two high speed video camera systems, depending lighting conditions, to capture in-flight fragmentation trajectories: 1) Photron SA-Z with a 24 mm lens and a resolution of 384 x 248 pixels at a frame rate of 150,000 frames per second (fps); 2) Phantom TMX with a 50 mm lens and a resolution of 1024 x 544 pixels at 110,000 fps. Each of the cameras was triggered by a breakwire embedded within the charge, allowing for accurate determination of the moment of detonation. Illumination of the event was provided by an LED light panel positioned as the background of the camera field of view.

3. Results and Discussion

3.1. Fragmentation recorded from witness panels

The results of the fragmentation witness panel analysis for different water levels are summarized in Table 1. Important to note is an incomplete data set for the 2.6 mm balls with trials conducted at limited depths to establish the validity of the findings across casing scales rather than testing each parameter due to testing restraints. The results of the witness panels will be discussed by casing type below.

Table 1. Average number of fragments and avg. % of steel mass recovered from witness panels.

Setup	Machined casing (% by weight)	1.7 mm balls	2.6 mm balls
		(% by weight/number)	
Air (A)	171 (11.3%)	286 (15.3%)	-
Half-submerged (B)	165 (11.9%)	322 (17.2%)	233 (26.7%)
Charge at surface (C)	118 (13,7%)	305 (16,3%)	-
60 mm depth (D)	11 (17.0%)	319 (17.1%)	164 (18.7%)
110 mm depth (E)	1 (1.2%)	2 (0.1%)	116 (13.3%)

Steel machined casing.

Across nominally identical trials, the machined steel casing produced fragments which varied significantly in mass and geometry. In the air detonations (Setup A), fragments size was smaller than for those recovered during water trials — occasionally up to 25 mm in length — yet detonations within air generated a greater quantity of fragments, mostly weighing less than 0.01 g. Fully submerged charges yielded the opposite trend: fewer fragments were recovered in the witness panels overall but of greater individual size (up to 55 mm). The heaviest single fragment from the machined casing weighed 1.7 g at 60 mm depth (Setup D), i.e., ~4% of the original casing mass, yet penetrated only two strawboard layers owing to a flat, large-area impact. Thus, higher kinetic energy is not directly proportional to greater penetration depths; penetration is also governed by the projectile's aspect ratio and impact angle. Given the high variability in fragment shapes produced by natural casing breakup, reliable prediction of maximum fragmentation range is feasible only from experimental evidence specific to the charge type under consideration. It is inconclusive to deduce whether the potential of smaller fragments in water, as well as the larger, occur due to the fact any smaller fragments may have failed to breach the water surface, and interact with the witness panel so were not recorded.

For the steel machines case submerged at 60 mm depth (Setup D), the average recovered steel mass of the fragment striking the panel was 6.3 g (17.0% of the original casing mass), compared with 4.2 g (11.3%) in air. The half-submerged configuration yielded 4.4 g (11.9%), and the subsurface charge 4.8 g (13.7%)—all exceeding the air case. It is hypothesised that in the air test, the directionality of the fragments is unaffected and therefore radial and so a large proportion of the fragments will never interact with the witness panel. The increase in recovered casing mass as depth of the charge increases, despite a reduction in individual fragment count, indicates the fragments are larger at greater depths.

The total recovered mass from the machined casing increased with burst depth up to 60 mm and then fell sharply to 0.45 g (1.2%) at 110 mm. The rise at 60 mm is attributed to strong bubble venting at shallow depth, which entrains and ejects numerous small shell fragments which at this depth were unable to eject the water through their own trajectory alone with the outflowing water, thereby increasing the material reaching the witness panel. At 110 mm, the bubble forms farther from the free surface and the venting impulse is much weaker; the longer water path and greater hydrodynamic drag retain fine debris within the water column, so fewer small fragments reach the panel and the recovered mass decreases.

Steel ball bearings.

To consider the flight of more idealistic fragmentation, the steel ball bearing were used, but to correlate these events to the machined casing an equivalent casing mass facing the witness panels was calculated. The use of ball bearings allows for an idealised flight measurement to be evaluated in that no energy is spent fracturing the casing itself, however due to being separate balls and spherical a less efficient transfer of energy occurs in comparison to the machined liners. For the standoff distance of 600 mm between the charge axis and the witness panel, approximately 18 % of the steel ball bearings were facing toward the panel (Figure 6). An axially initiated charge in setup (A) gives a theoretical number of 332 (1.7 mm) and 156 (2.6 mm) fragments which should impact the witness panel, assuming an ideal radial trajectory and perfect casing packing. Considering the 1.7mm trials, after the air detonations, an average of 286 small steel balls were recovered from the witness panels corresponding to 15.3 % of the total steel mass. This was an appropriate recorded value due to some fragments interacting directly with the mounting frame which partially obscured the witness panel. The greater number of fragments for setups B, C and D (17.2 %, 16.3 %, 17.1 %) is attributed to the presence of water and its influence on fragmentation velocity and distribution in a similar methodology as discussed for the steel machined casing.

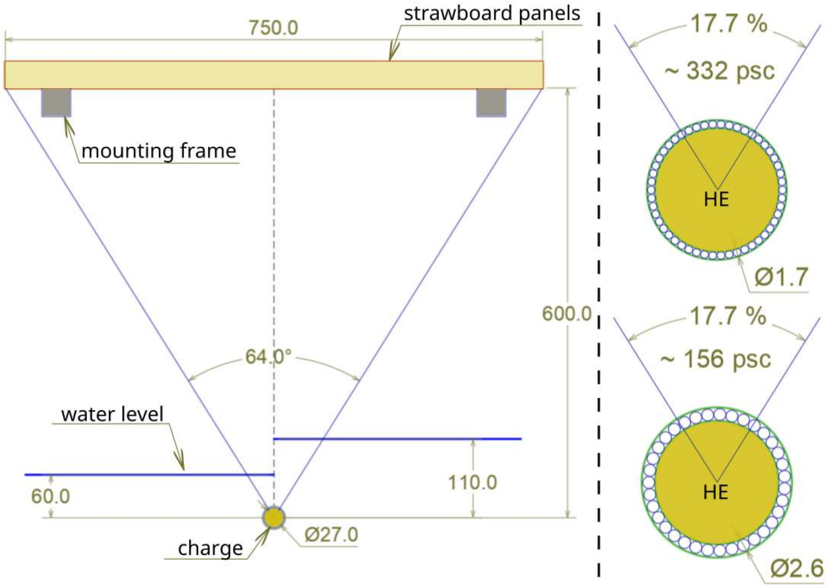

Figure 6. Schematic side-view of the test setup – the witness panel for 60 mm and 110 mm submerge and cross-section of cased charges with ball bearings.

The influence of water was more significant for the larger 2.6mm diameter balls, where in setup B the number of recovered fragments increased to 233 (by 49 %) compared to the predicted 156 fragments for an air-blast (~18% presented in Figure 6). A similar phenomenon was hypothesised here in that larger balls were not able to eject from the water, due to increased hydrostatic drag, and therefore were carried by the late-time bubble expansion and collision with the witness panel.

Figure 7 shows the recovered 1.7 mm and 2.6 mm steel ball bearings. Despite localised flattening on the face nearest the explosive, the spheres retained their geometry, with average mass loss not exceeding 3%, which is essential for subsequent velocity and energy analyses. As each projectile has a nominally constant mass (~0.02 g for 1.7 mm; ~0.07 g for 2.6 mm), the number of impact marks on the first witness panel provides a direct estimate of the total mass of fragments striking the target.

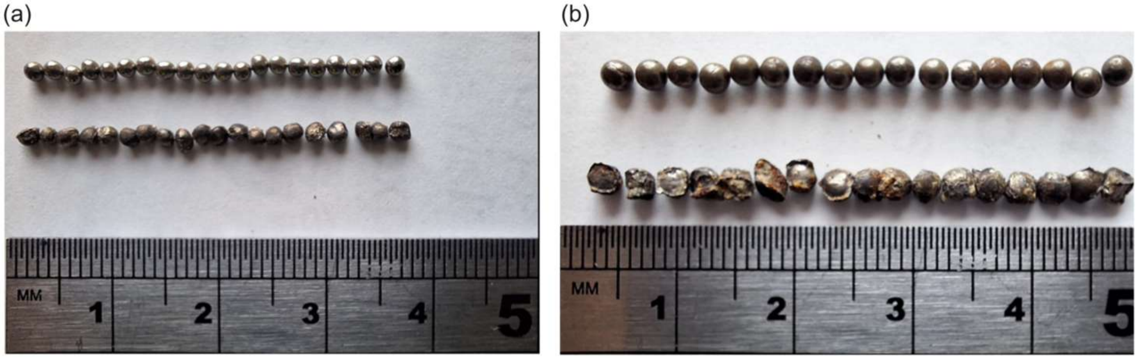

Figure 7. Recovered (a) 1.7 mm and (b) 2.6 mm steel ball bearings showing limited local deformation on the contact side; overall shape and mass remained unchanged.

Figure 8 illustrates the typical fragment density patterns recorded on the witness panels for the machined steel casing detonations conducted in air (a, b) and with the charge top positioned at the water surface (c, d). The coloured background represents fragmentation regions on the panel, corresponding to the nose (green), tail (yellow, detonated end), and central (blue) sectors, with red zones marking the panel's geometric limits. A notable reduction in the total number of fragments—from 190 in air to 124 under surface conditions—was observed, demonstrating the attenuating influence of water on deaccelerating fragmentation to reduce likelihood of breaching the water surface. For comparative clarity, fragment distributions are presented in both Cartesian (a, c) and polar (b, d) coordinate systems, referenced to the charge centre and the angular position relative to the nose. In each plot, red lines and markers indicate impacts on the right-hand side of the panel, whereas blue denote those on the left. The unobservable area (contoured by black lines) corresponds to shadowed areas outside the field of view. A complete dataset of fragment densities for all three casing types and the maximum number of fragments recovered in each test configuration is provided in Appendix B.

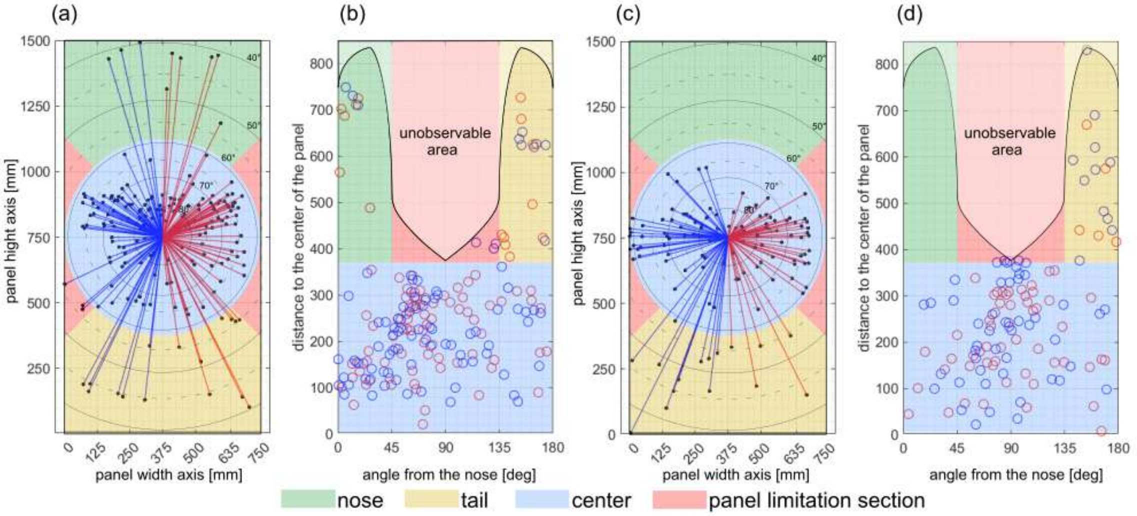

Figure 8. Fragment density maps with colour-coded panel sections for machined steel casing detonations conducted in air (a, b) and with the charge top positioned at the water surface (c, d). In the polar plots (b, d), 0° corresponds to fragments projected forward from the nose of the charge, whereas 180° represents fragments ejected rearward from the tail.

For all three casing types, the light-blue sector corresponds to the region of highest impact density, associated with large launch angles (~59–90° to the charge axis) and hence short trajectory distances prior to impact. The light-red sector denotes the lateral limitation region. As the panel width is 750 mm, relatively few strikes are recorded laterally (Figure 8b, d); additional impacts are expected beyond the panel edges however due to testing limitations were not captured. Across all tests, impact fields are approximately symmetric about the panel centreline, with the dominant concentration in the central zone. The tail sector (yellow) consistently exhibits more hits than the nose sector (green). The reduction at the nose is attributed to greater standoff from the initiation point and additional energy release at the rear resulting in a net flow of energy from tail to nose, and thus fragment trajectory at the nose being affected.

When considering Figure 8b and 8d, the influence of water on fragmentation behaviour is evident. Increasing submersion depth significantly reduces both fragment number and velocity due to hydrodynamic drag associated with non-idealistic fragmentation shape and energy dissipation within the water column. With the explosive charge at 110 mm depth (scaled depth 0.29 $m \cdot kg^{-1/3}$), fragment counts decrease by approximately 99% for the machined casing and 1.7 mm ball-bearing configurations, and by around 50% for the 2.6 mm ball bearings.

3.2. Evaluating fragment velocities from high-speed video imaging

The total recovered steel mass within the witness panels provided a reasonable indication of the amount of casing material ejected but offers limited information on directional hazard. At 110 mm, the risk of above-surface fragmentation presented was minimal; however, for shallower charge positions, panel data alone is insufficient to define safe operating distances. Therefore, to improve assessment accuracy for real-world events, a high-speed image-based fragment-tracking method was developed to quantify fragment velocity, trajectory and range.

Figure 9 presents an individual HSV frame from each of the three different fragmentation casings at different depths to show indicative expansion behaviours. A balance of shutter speed and additional lighting was the key during these trials to ensure the quality of HSV imagery in both over-exposed and low-light conditions in air and submerged trials respectively.

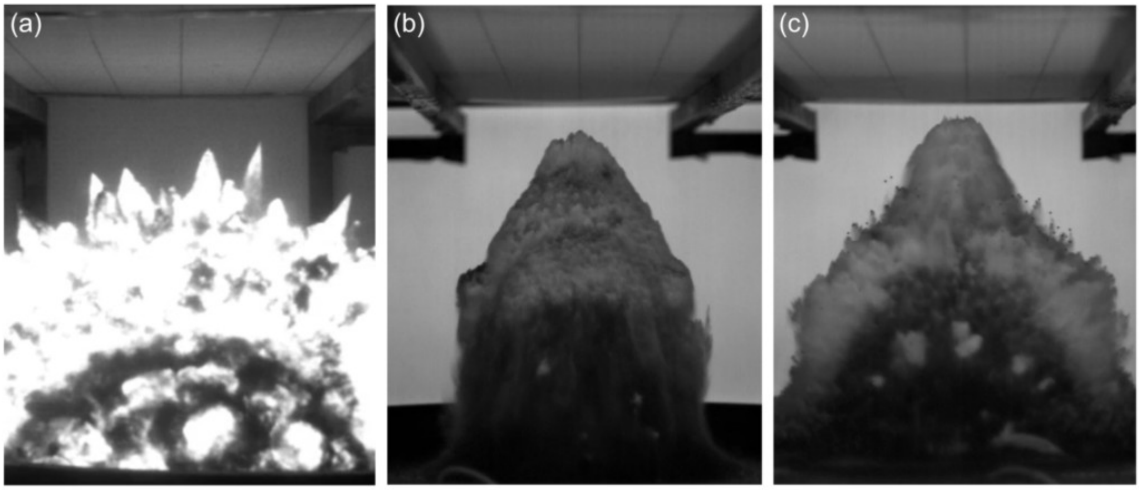

Figure 9. High-speed video (HSV) recording snapshots showing a range of casing and depth combinations, for illustrative purposes: (a) 1.7 mm balls in air (A), (b) machined casing at 60 mm (D) and (c) 2.6 mm balls at 110 mm (E).

A MATLAB script was created to track fragment positions from the detonation point within successive video frame images to evaluate the distance of travel. Extracting a real-world measurement of fragment trajectory from the HSV images required a calibration image (with a physical distance marker in view of the camera) to establish the size of a given pixel within each frame. The distances, evaluated from the assumed charge centre (at 600mm below the centre of the witness panel), were stored with respect to time, with this relationship being used to estimate fragmentation velocity. This process assumed a 2-D plane of fragments around the charge circumference and therefore can underestimate the travel distance and the fragment velocity of fragments travelling out of plane. However, as seen in Figure 8, this planar assumption appeared reasonable for a large proportion of the fragments, evidenced by the narrow banding of many of the impacts on the witness panel.

Image subtraction was utilised to identify differences between subsequent video frames. To account for camera sensor noise resulting from lighting fluctuations, a pixel intensity thresholding was implemented, following the approach proposed in Farrimond et al. (2022). The region of interest above the charge was discretised into 5° sectors to locate tracked fragments which may not travel along perfect radial spokes from the detonation point. It was assumed that the furthest point of difference in the image in each sector should be taken as an ejected fragment. HSV frames from an example test are shown in Figure 10, with the selected ejecta front fragments highlighted by red circles.

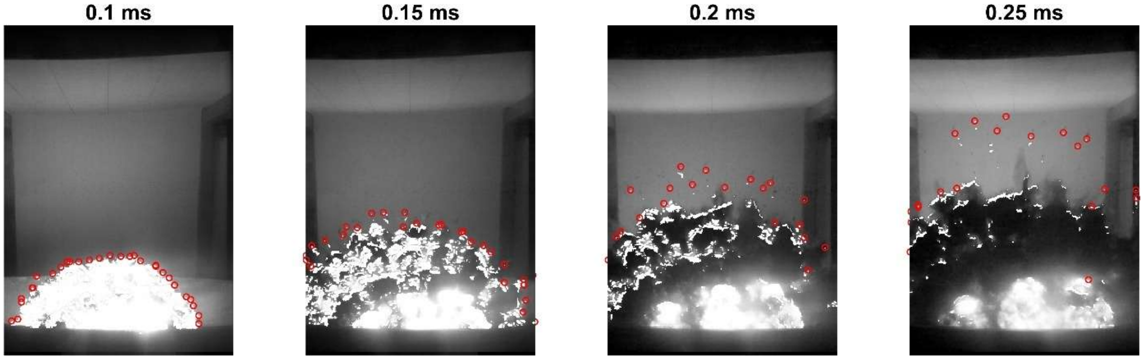

Figure 10. Automatic fragment tracking (red circles), using high-speed video processing of the machined casing detonation in air.

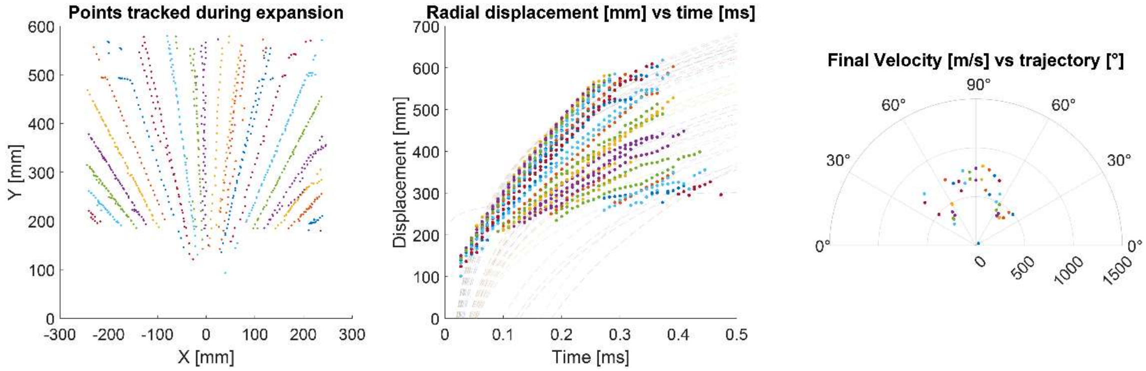

Figure 11. Exemplary fragment tracking of two 1.7 mm ball bearing tests with water level aligned to charge top, setup C, to show consistency, with the trajectory rounded to nearest 5 degrees: (a) points tracked during expansion, (b) radial displacement vs time and (c) final velocity vs trajectory.

Figure 11a represents the tracked fragmentation position during its trajectory and prior to interacting with the witness panel. Each individual point of colour represents each 5° sector and then its development in time. This data was manipulated to create an indicative distance with respect to time plot as seen in Figure 11b. A log fit was used to characterise the initial velocity of the fragments as they were accelerated by the charge, followed by the deceleration due to air and water resistance effects. In the two 1.7 mm ball bearing examples shown in Figure 11, generally, higher fragment velocities for those travelling vertically above the charge were recorded than fragments with horizontal travel vectors. The ‘final velocity’ is defined as the fragment velocity evaluated at 550 mm vertically away from the charge centre (i.e. immediately prior to witness panel impact) and is plotted with respect to trajectory angle in Figure 11c.

Figures 12a-e present the results of all the 1.7 mm ball bearing trials at each level of submersion with results showing that increasing depth of water above the charge results in a decreasing velocity of fragments, and that final velocity decreased as the launch angle deviated from 90°. This is a key fundamental finding for safety operational guidance, as it suggests when a charge is significantly below the water surface, the higher velocity fragmentation breaching the water surface is limited to mostly vertical trajectories. The general conclusions of launch angle and velocity reduction held true across all casing types as they were submerged under water.

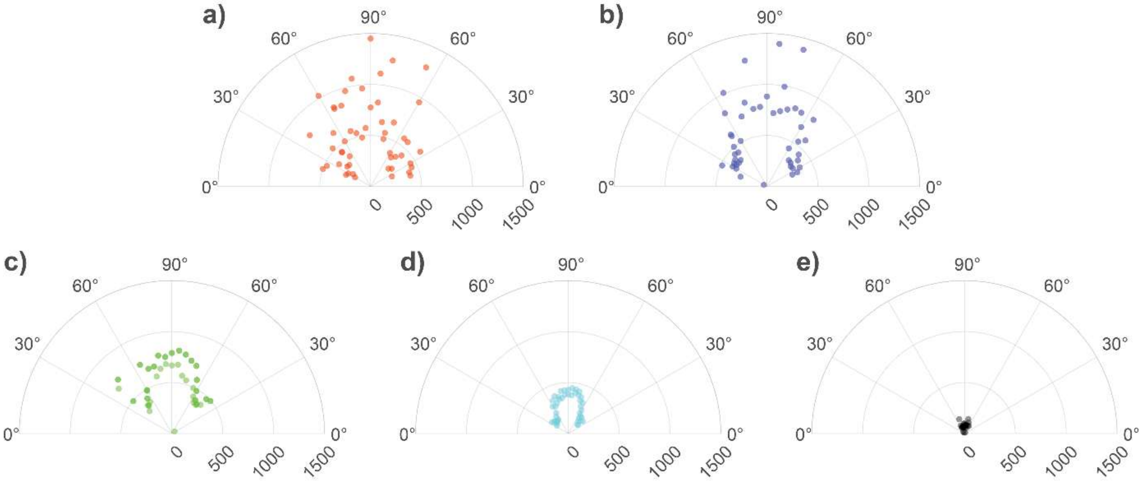

Figure 12. Final velocities (m/s) of fragments from 1.7 mm bearing tests with varying levels of submersion: (a) air (no water), (b) half-submerged, (c) charge top at surface, (d) 60 mm depth and (e) 110 mm depth.

3.3. Existing empirical prediction comparisons

3.3.1. Gurney Equations

Although fragment flight characteristics for the three types of charge casings were tracked using high-speed video (HSV), only the pre-formed steel balls maintained a consistent size and shape, enabling the assignment of mass to individual tracked fragments. In these cases, kinetic energy was estimated. In contrast, the monolithic steel liner disintegrated into irregular fragments during detonation. Upon impact with the witness panel, these primary fragments often underwent further break-up, which hindered detailed analysis.

The Gurney model (1943) is frequently used to estimate metal casing fragment velocity following an explosion. The model assumes the explosive energy is converted to kinetic energy that breaks up the metal case and imparting momentum to the fragments. For a cylindrical charge (Charron 1979) of known mass and type of explosive material, and the mass of the high-strength steel casing, the initial fragment velocity v_o (m/s) can be calculated from Equation (1).

$$v_o = \frac{\sqrt{2E}}{\sqrt{\frac{m_s}{M}+0.5}}, \tag{1}$$

where $\sqrt{2E}$ is the Gurney constant, M is the mass of the explosive, and m_s is the mass of the steel casing.

Table 3 presents properties and the Gurney constants for TNT- and PETN-based explosives. The Gurney constant for PE10 can be estimated using a simple correlation (Equation 2) proposed by Cooper (1997), which relates the constant to the detonation velocity of the high explosive material. The value of 2605 m/s fits well in Table 3 between PETN and SEMTEX 1A and therefore provides confidence in the values presented by Farrimond at al. (2024).

$$\sqrt{2E} = \frac{D}{2.97} = \frac{7735}{2.97} = 2605\ [m/s] \tag{2}$$

Table 3. Properties of high explosives.

Explosive	TNT equivalent	Density [kg/m^3]	Detonation Velocity [m/s]	Gurney Constant [m/s]
TNT	1.0	1.61	6900	2438
PETN, (Frem 2023)	1.27	1.78	8260	2926
PE10 (86% PETN), (Farrimond et al. 2024)	1.22	1.55	7735	2605 (2)
SEMTEX 1A (83% PETN), (Fan et al. 2023)	1.13	1.47	7318	2587

In the machined casing tests, the extracted velocities extracted from HSV cannot be linked to appropriate fragments and their masses due to their irregularity. However, in the ball bearing tests each fragment has a near-identical mass both prior and after the trial so the velocity data was appropriate for further fragmentation analysis using the Gurney model to evaluate the fragment velocities. As the fragment tracking area was discretised into 5° sectors, in some cases the coordinates of more than one fragment per sector were collected. This resulted in the recording of a small number of distorted and unrealistic velocity values (at velocities greater than the maximum shown in Figure 12), which could be identified and ignored as outliers using the Gurney-predicted velocity, v_o. The ball bearings enclosed in the weak 3D-printed jacket allowed for easier venting of the detonation products, which should result in a lower velocity than that calculated in Equation 1. Using the Gurney model and assumptions provided by Cooper (1997) and Li et al. (2024) for weaker casings, predictions in the maximum velocities achievable are evaluated for the trials presented within this article and noted in Table 4.

Table 4. Fragment initial velocities for steel balls casings and 46.5 g PE10 charge.

Type of casing	v_o (1.7 mm)	v_o (2.6 mm)
high tensile steel	2268	1936
preformed shells 90 %*v_o[a]	2041	1743
brittle iron 80 %*v_o[b]	1814	1549

[a, b] Data obtained from (Cooper 1997; Li et al 2024).

Referring to the Gurney predictions for each ball size, assuming 80% of the energy is retained during the reported trials, the velocities captured from the HSV analysis that exceed 1814m/s and 1549m/s for 1.7mm and 2.6mm balls respectively are assigned as outliers and ignored. The corrected fragment velocities for 1.7 mm (a) and 2.6 mm (b) ball bearings at 550mm standoff are presented in Figures 13a-b. Each test group of velocity–angle measurements was fitted with a polynomial trendline to capture the nonlinear variation of velocity across measurement angles. The plots do not represent a theoretical model of the physics but rather a mathematical approximation that smooths the scatter of points and highlights the overall pattern for each test condition.

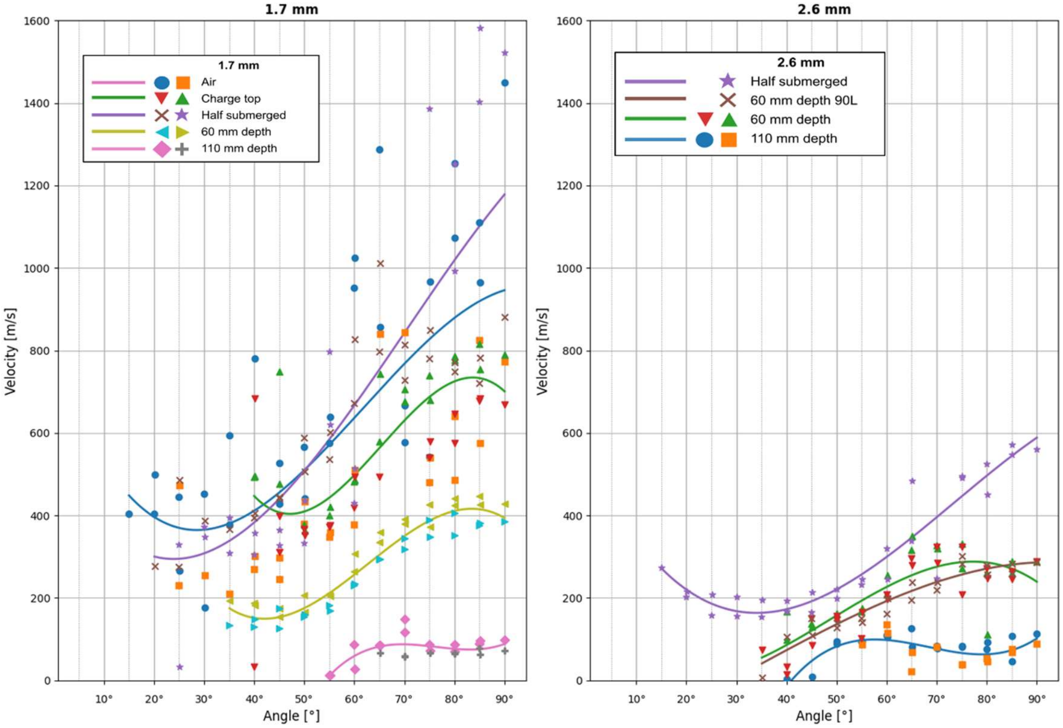

Figure 13. Fragment velocities at 550 mm standoff vs launch angle for 1.7 mm (a) and 2.6 mm (b) balls.

3.3.2. McMahon velocity evaluation

The depth of penetration of the strawboard panel can be correlated to a strike velocity according to the empirical equations presented by McMahon (1971). The relevant equation for regular fragments is as below:

$$Vs = 337\ \frac{P}{M^{\frac{1}{3}}\rho^{\frac{2}{3}}} +\ 205 \tag{3}$$

where: Vs is the strike velocity (215 to 1400 m/s), P is the thickness of strawboard penetration, (number of layers x 3.7 mm), M is the fragment mass (20.4mg for 1.7mm balls) and ρ is the fragment density (7.8 g/cc).

This equation operates under an assumption that fragments travel at 1400 m/s or below, as above that the velocity of impact with the strawboard is likely to cause fragment deformation (resulting in a lower penetration than in an undeformed state). Using Equation 3, and the accompanying strawboard witness panel penetration data recorded in section 3.1, a final strike velocity of the steel ball fragments was be evaluated based on how many balls penetrated each layer; presented in Figure 14 is each tested scenario with the 1.7 mm ball bearings. When comparing the spread in the final velocities between the HSV recordings (Figures 12a-e) and the strawboard analysis (Figure 14), which have been coordinated with colour for test type, there is a clear agreement between the two methods of inferring in-flight velocity at impact. For instance, in the 110 mm depth to charge centre (setup E) both methods suggest an impact velocity of all fragments at 300 m/s or below. Similarly with Setup A, B and C when comparing both methods, there is a much larger spread in the velocities recorded but exhibit an average value of around 800 m/s which aligns with the results in Figure 14. This comparable data across each scenario co-validated both McMahon (1971) strawboard witness panel analysis for regular shaped fragments and the novel HSV methodology presented in this article.

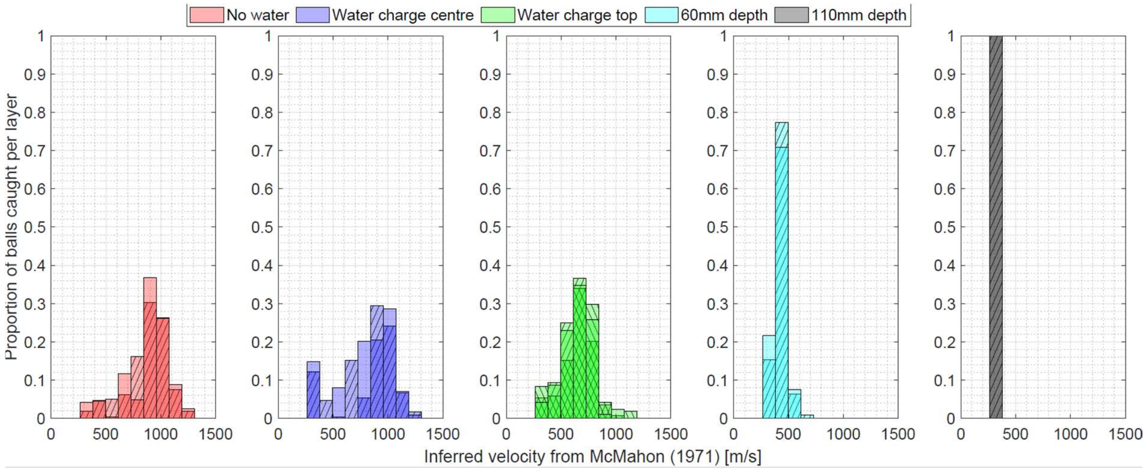

Figure 14. Inferred velocity of 1.7mm ball fragments at impact on strawboard witness panels based on equations presented by McMahon (1971), whereby the different hatch styles represent nominally identical tests to visually represent consistency.

3.4. Maximum fragmentation range and injury criteria

The centre point of the first witness panels was located 600 mm above the charge for all the tests conducted within this study. The position of the fragmentation holes in the witness panels can be described in a three-dimensional coordinate system with the charge located at the origin (0,0,0). The points on the first witness panels (x_i,y_i,z_i) were converted into the spherical coordinates (ρ_i,θ_i,φ_i), where i denotes the fragment number, ρ_i is the distance to the origin ($0< \rho_i$), θ_i is the angle at x-y plane ($0< \theta_i <360°$) and φ_i is the angle at z-y plane ($0< \varphi_i <90°$). α_i is the angle in z,r_i plane and takes $\alpha_i = 90° - \varphi i$. The final velocities obtained from the high-speed video (HSV) at an offset of 550 mm from the detonation point, as presented in Figures 12a-e and 13a-b, were used further to estimate fragmentation range. The fragment impact positioning presented in Appendix B, were then projected onto the surface of a hemisphere, defined by the spherical coordinates ($550, \theta_i, \varphi_i$), as shown in Figures 15a-b. The movement of a fragment was recorded as a 2D image on the z-y plane, which results in differences in the recorded velocities depending on the angle values θ_i and φ_i.

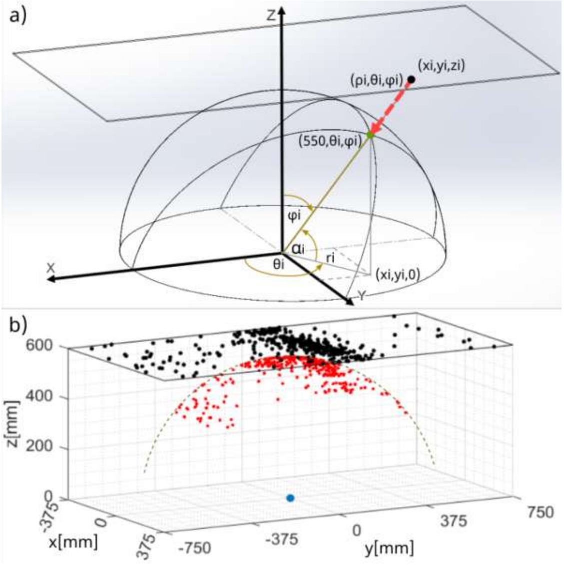

Figure 15. Projecting the witness panel coordinates on a hemisphere (a) scheme and (b) data from a measurement of the case with 1.7 mm balls (black dots represent fragment positions at witness panel, while red dots represent its 550 mm hemisphere counterpart coordinates).

Most of the fragments hit the witness panel at the launch angle α larger than 50° - assuming that 90° is vertical direction. The maximum fragmentation range for submerged charges depends on the launch angle and the distance it travels within the water. A shorter distance means lower fluid resistance and higher velocity at the surface. Obviously, for α around 90°, the initial velocities of ball bearings should be the highest, and the horizontal shift from the origin ri(α) is minimal. To quantify the density of fragment distribution, the z-y plane was divided into 3 intervals, for launch angles α equal to 0-50°, 51-70° and 71-90°. In those intervals, the maximum velocities at 550 mm standoff were used for fragmentation range calculation (Table 5).

Table 5. Steel balls maximum velocities at predefined launch angle intervals.

	Ball diameter	**Test setup**	**Max. velocities at launch angle [m/s]**		
			0-50°	**51-70°**	**71-90°**
1	1.7 mm	(A) air	780	1287	1450
2	1.7 mm	(B) half-submerged	588	1012	1582
3	1.7 mm	(C) charge top at surface	749	743	815
4	1.7 mm	(D) 60 mm depth	205	391	446
5	1.7 mm	(E) 110 mm depth	0	149	97
6	2.6 mm	(B) half-submerged	221	483	572
8	2.6 mm	(D) 60 mm depth	167	350	331
9	2.6 mm	(E) 110 mm depth	95	135	113

Based on the coordinates at the witness panels, velocities from the HSV processing, and fragment mass as well as its shape, the individual flight trajectories and fragment ranges were calculated. A classical system of equations of motion, presented in Equation (4) was used to predict the steel ball bearings flight trajectory and their energy during flight (Sielicki et al 2021).

$$\left\{ \frac{d^2r}{dt^2} = \frac{C_dA\rho}{2m}\sqrt{\left(\frac{dr}{dt}\right)^2 + \left(\frac{dz}{dt}\right)^2}\,\frac{dr}{dt} \qquad \frac{d^2z}{dt^2} = -g - \frac{C_dA\rho}{2m}\sqrt{\left(\frac{dr}{dt}\right)^2 + \left(\frac{dz}{dt}\right)^2}\,\frac{dz}{dt} \right. \tag{4}$$

With the changing velocity, it is necessary to update the sphere's drag coefficient during numerical calculations. The Equation (5) given by Morrison (2016) accounts for the drag coefficient, C_d, at the dimensionless Reynolds number up to 10^6.

$$C_d = \frac{24}{Re} + \frac{2.6\left(\frac{Re}{5.0}\right)}{1 + \left(\frac{Re}{5.0}\right)^{1.52}} + \frac{0.411\left(\frac{Re}{2.63\,\times 10^5}\right)^{-7.94}}{1 + \left(\frac{Re}{2.63\,\times 10^5}\right)^{-8.0}} + \frac{0.25\left(\frac{Re}{10^6}\right)}{1 + \left(\frac{Re}{10^6}\right)} \tag{5}$$

The relation between flight velocity v and Reynolds number Re, Equation (6), can be written in the following form (Landau & Lifshitz 1987):

$$Re = \frac{\rho_{Air}Dv}{\eta} \tag{6}$$

where ρ_{Air} is the air density, D the characteristic length of a flying object (i.e. diameter for the sphere) and η represents the dynamic viscosity of the air at a defined pressure and temperature. For a maximum velocity presented in Table 5, the highest Reynolds number reaches 177,000 corresponding to the drag coefficient C_d equal to 0.41.

Fragment trajectory and energy are key parameters in estimating tissue damage and lethality from fragment impacts. Certain values of overpressure and impulse can cause tissue damage and death, but, as shown by McCleskey et al. (1990), the consequences of the kinetic energy of a projectile or fragment may also be lethal. In military and governmental publications, the rule of 78-80 J or greater for blunt trauma (Zaker 1975; Department of Energy 2012; Department of Defence 2024) is the standard for hazardous fragment energy for personnel. However, the energy value mentioned by Rohne (1906) neglects important factors such as the shape, size, body location, and surface area of the projectile upon impact, all of which influence its potential to cause damage or injury. The tests conducted in this study with steel ball bearings (masses of 0.02 and 0.07 g, respectively) have minimal lethal potential, but still under favourable conditions, objects of such small sizes can cause minor or serious injuries. A more realistic model for determining the anticipated harm from a fragment impact is presented in equation (7), based on energy density:

$$\frac{E}{A} = \frac{E_K}{A} = \frac{mv^2}{2A} \tag{7}$$

where: E/A – energy density [J/cm^2]; E_K – kinetic energy [J]; A – cross-sectional area [cm^2] at the target ($A = \pi r^2$ for spherical projectiles); m – mass and v – fragment velocity.

The maximum kinetic energy of the ball bearings at a 0.55 m standoff is 25.5 J for 1.7 mm and 11.4 J for 2.6 mm balls, obtained from the highest recorded velocities given in Table 5. A common injury criterion for those fragments is related to skin penetration and soft tissue damage. Minimal velocities for both sphere sizes and energy criteria obtained from Whiting (2011) and Foley (2023) are shown in Table 6. Those velocities will be used in this study as injury criteria during fragment flight.

Table 6. Minimum velocities required for tissue damage by 1.7 mm and 2.6 mm steel ball bearings, based on the energy-density criterion.

	Organ	E/A criterion [J/cm^2]	E_K [J] (1.7 mm) (2.6 mm)	v_{min} [m/s]
1	Eye penetration [a]	5.0	0.11 0.27	105.5 87.2
2	Skin perforation [a]	12.5	0.28 0.66	166.9 137.9
	50 % risk of skin penetration [b]			
3	Femur	12.62	0.29 0.67	167.7 138.6
4	Abdomen	18.7	0.42 0.99	204.1 168.7
5	Anterior between ribs	22.3	0.51 1.18	222.9 184.2
6	Lower back	28.6	0.65 1.52	252.4 208.6
7	Scapula	33.3	0.76 1.77	272.4 225.1
8	Posterior torso on ribs	34.3	0.78 1.82	276.4 228.4

[a,b] Data obtained from (Whiting 2011; Foley et al 2023).

The tests which utilised steel balls as the fragmentation mass (17 tests) and Equation (4) were used to calculate the fragmentation distance assuming no obstacles or obstruction were present. Figures 16a-b visualizes flight trajectories and fragment distribution with injury colour coding based on energy density criteria and minimum injury velocity presented in Table 6. The flight prediction used initial velocities for three predefined launch angle intervals from Table 5, to obtain a worst-case scenario for each test. All fragmentation flight trajectories are gathered in Appendix C for reference. In one 1.7 mm steel ball test, no fragmentation was observed for the depth of 110 mm. The colours indicate the maximum distance for which a fragment possesses sufficient kinetic energy (velocity) to cause damage according to four injury criteria shown in Table 6: eye penetration (green - 5.0 J/cm^2), skin perforation (orange - 12.5 J/cm^2), 50 % risk of skin penetration at the abdomen (red - 18.7 J/cm^2) and scapula (black - 33.3 J/cm^2) regions.

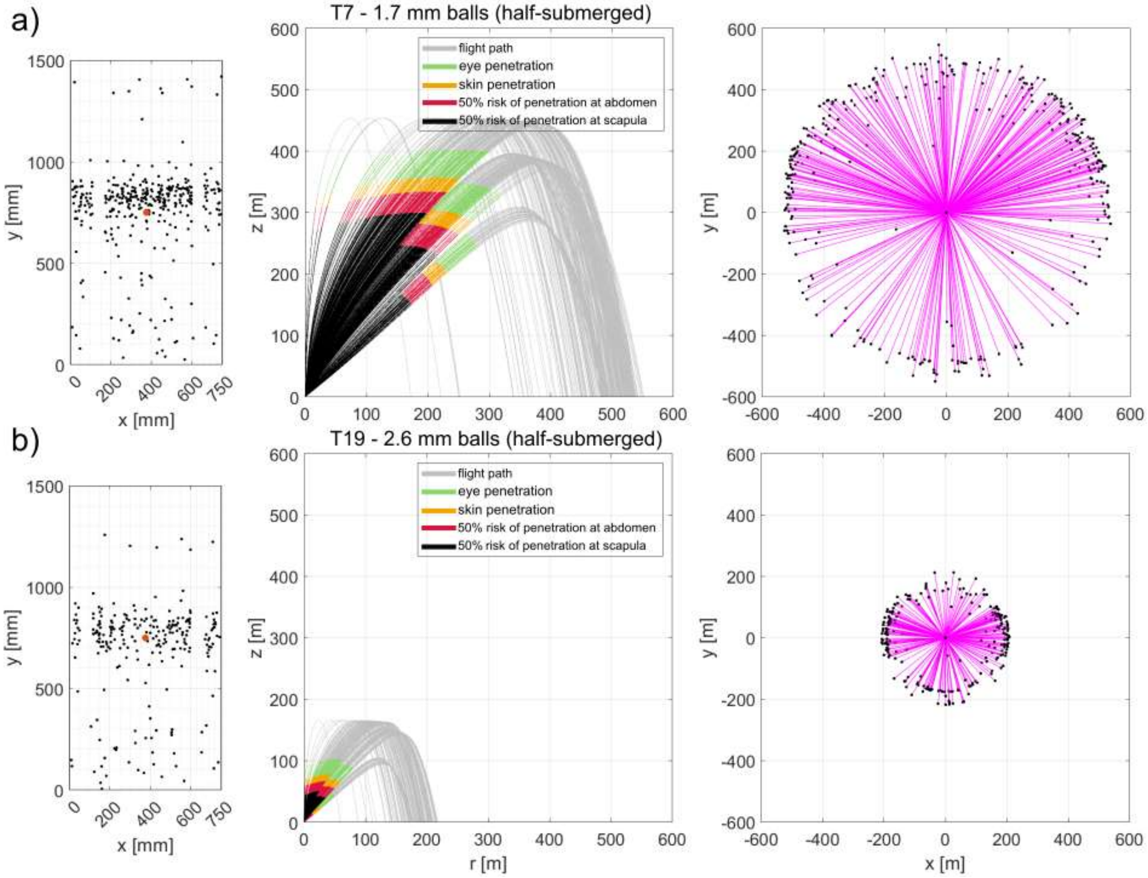

Figure 16. Witness panels fragmentation pattern (left column), flight trajectories of all fragments considering selected injury criteria (centre column) and fragmentation distance in plan view (right column) for the half-submerged charge (setup B): (a) 1.7 mm and (b) 2,6 mm.

Based on flight trajectories, Table 7 presents the predicted probabilistic maximum fragment range (distance where a fragment reaches the ground level after explosive ejection) and hazardous distances for the proposed injury criteria. Important to emphasise is these are estimates based on small-scale experiments and should be used with caution as there is still chance of extreme fragmentation (i.e of mass, velocity, shape, launch angle) which could significantly exceed these. The worst-case scenario from this probabilistic analysis is considered (i.e. highest velocity from the angle intervals) however, in reality, a small number of fragments will extend this far with a minimal probability of wounding a person. At larger distances, the surface area of the hemisphere that a fragment can hit is larger, in relation to fragment projected area.

Using the half-submerged charge as a reference, a reduction in fragmentation range with depth is observed. At 60 mm depth the maximum fragment distance is reduced by 24 % (for 1.7 mm balls) and 9% (for 2.6 mm balls) and at 110 mm depth by 82 % and 36 %, respectively. For the proposed injury criteria even higher reduction of hazardous distance for both steel balls size can be observed. Projectiles thrown from a depth of 110 mm have low velocities and therefore pose little risk of skin penetration.

Table 7. Predicted maximum fragmentation range and distance with injury criteria in meters.

Setup	Max fragment range [m]	Eye penetration [m]	Skin penetration [m]	50 % risk of skin penetration for	
				abdomen [m]	scapula [m]
			1.7 mm balls		
Air	583	345.3	296.6	273.7	240.4
Half-submerged *	551.7	321.1	272.5	249.7	216.2
60 mm depth (% reduction)	419.9 (23.9%)	212 (34.0%)	163.9 (39.9%)	141.5 (43.3%)	108.7 (49.7%)
110 mm depth (% reduction)	98,8 (82.1%)	10,8 (96.1%)	1,3 (99.5%)	negligible risk	negligible risk
			2.6 mm balls		
Half-submerged *	217.4	82.0	59.1	49.2	35.1
60 mm depth (% reduction)	198.7 (8.6%)	66.7 (18.7%)	44.1 (25.4%)	34.3 (30.3%)	20.1 (42.7%)
110 mm depth (% reduction)	138.7 (36.2%)	20 (75.6%)	negligible risk	negligible risk	negligible risk

* used as reference

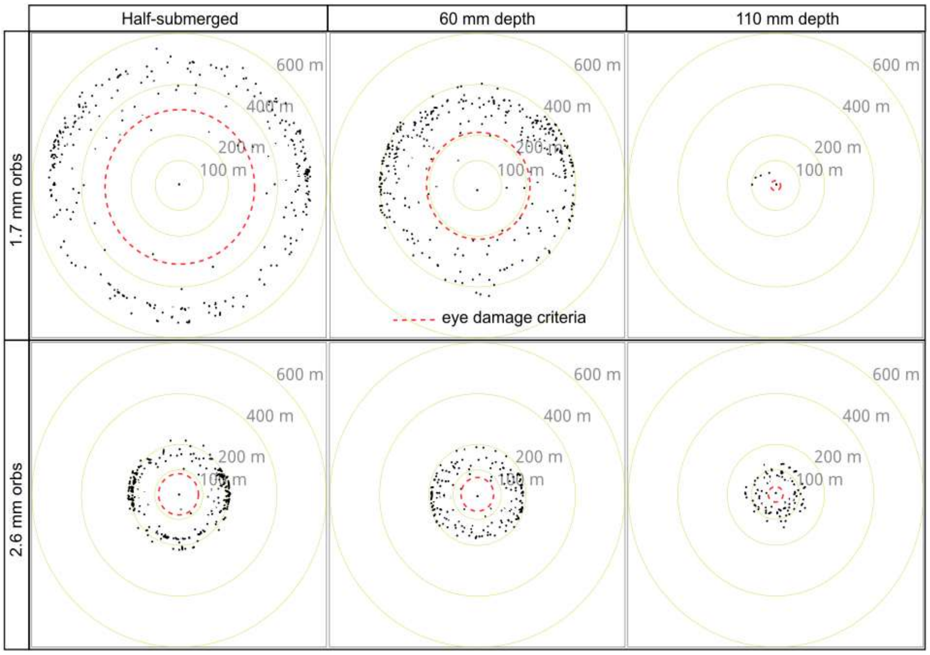

Figure 17. Distribution of maximum fragment range and eye damage criteria for charges with different depth.

Calculating the flight trajectory from the fragment traces and with variable drag coefficient enables the comparison of fragmentation patterns at different depths as presented in Figure 17. At greater depths, the smallest fragments with lower mass were stopped under the water surface. This behaviour is visible also during the steel machined casing tests, where at 60 mm depth, 17 % of the recovered metal mass came from 11 fragments.

At the depth of 110 mm, the maximum fragment distance was reduced by 82 % for 1.7mm balls and by 36 % for 2.6 mm balls. Although the fragmentation distance of 99 and 139 m for steel balls submerged at 110 mm is significant, after only 11 m and 20 m (for the 1.7 mm and 2.6 mm steel balls respectively) they lose the ability to penetrate the skin and pierce the soft tissues of the eye (causing negligible lasting harm). In the study, the trajectories were not calculated for the machined casing because the obtained fragment velocities could not be assigned to a specific mass recovered from the witness panel.

3.5. Scaling fragmenting from small charges to full scale scenarios

Maximum fragment distance, minimum safe distance, and public withdrawal distance are terms used to describe the separation from an explosive device that ensures a desired level of safety. On land, the lethal shell fragments can travel beyond the critical distance associated with air-blast effects. Multi-mode hand grenades, such as the DM51 (Diehl Defence 2010), take advantage of this by employing a fragmenting sleeve to increase the lethal radius. In contrast, separation distance for submerged charges in relation to fragmentation hazards is generally not defined or considered in practice.

Swisdak and Montanaro (1992) proposed a method for predicting fragment behaviour for submerged munitions based on six trials with 500 lb general purpose bombs (Fig. 18). For an MK 82 bomb detonation at a depth of 0.69 m (scaled depth 0.14 m/kg $^{1/3}$), which approximately corresponds to the 60 mm test (at 0.16 m/kg$^{1/3}$) within this study, an 800 g fragment was recovered at a maximum distance of 594 m, closely matching the TRAJ (Montanaro 1990) program calculation of 595 m. The maximum fragment range for a single MK 82 detonation on land according to US military standards (Department of the Army 2011) is 969 m. According to this limited study, the 0.69 m of water reduced the maximum shell fragmentation distance for this ordnance filled with 87 kg of H-6 explosives by 39 %.

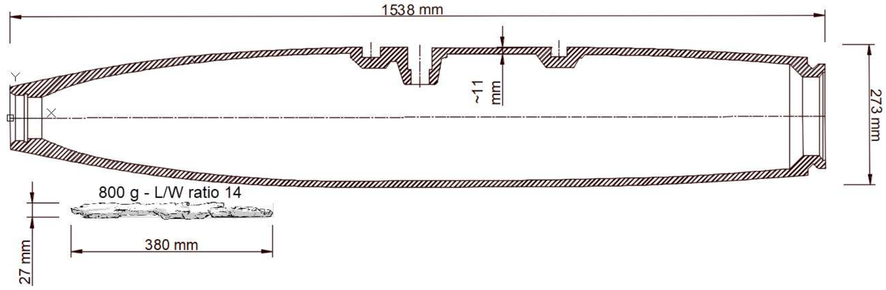

Figure 18. MK 82 bomb body and approximate size of an 800 g fragment mentioned in (Swisdak & Montanaro 1992).

In this study, the fragment velocities recorded from HSV were also compared against the work of Swisdak and Montonaro (1992) in order to determine the suitability of scaling up from small charges to full scale scenarios. Figures 19a-d shows data from this study (converted to scaled centroidal depths of burst) with curves of Swisdak and Montanaro overlaid. PE10, as used in this study, is known to have equivalent behaviour to PE4 (Farrimond et al 2024) nominally identical to C4, so a 1.02 velocity factor has been applied to the curves of Swisdak and Montanaro. Figures 19(a) and 19(c) contain the full data from all casing types, across all tested depths, with an azimuth of 0 degrees defined as vertically above the charge. Figure 19(b) and 19(d) show the mean velocity at each angle for each configuration of charge casing and depths of 60 mm and 110 mm, corresponding to scaled depths of 0.16 m/kg$^{1/3}$ and 0.29 m/kg$^{1/3}$, normalised by the vertical velocity for each series.

Presented are 'final' velocities recorded (extracted at 550 mm from charge centre) in Figure 19(a) which are considerably below the empirical curve. Additionally, there is reasonably high variability between velocities at varying azimuth values at this distance from the charge, as in Figure 19(b). This suggests that a substantial amount of deceleration has already occurred by the point of impact, highlighting the importance of ensuring that measurements are taken close to the water surface, especially when testing at reduced scale. When the polynomial curves developed in this study are used to extract velocities at a distance of 200 mm from the charge, the obtained results generally follow the trends presented in the Figures 19(c) and 19(d). However, significantly higher velocities were observed in this test series, alongside a more rapid decrease in velocity with increasing azimuth which could be related to the 2D analysis of the fragmentation tracking. Further work is required to assess the validity of the velocity extraction at this near-charge position, however the correlation with full-scale work is promising. These results provide the basis for developing and improving safe operation guidelines through validated experimental trials, removing the need for expensive and high-risk large-scale trials.

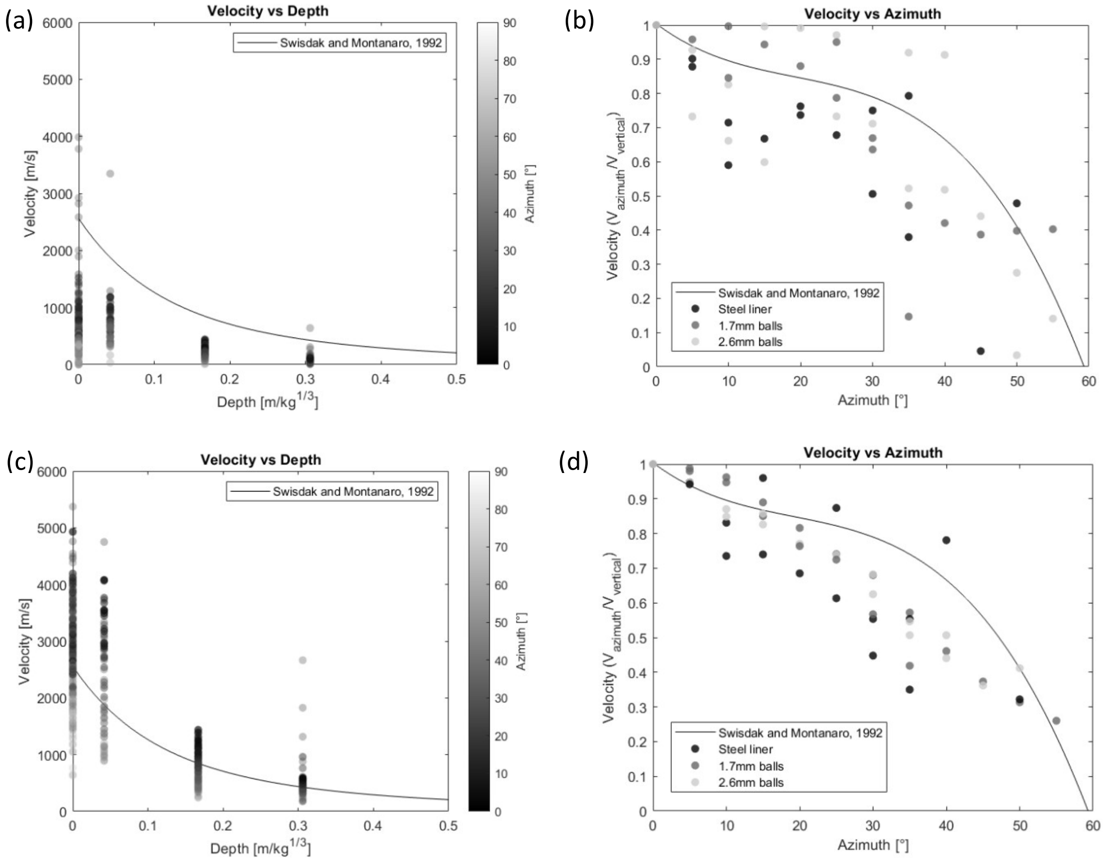

Figure 19. Fragment velocity data extracted at 550 mm (a), (b) and 200 mm (c), (d) from the charge centre versus curves of Swisdak and Montanaro (1992).

4. Conclusion and Recommendations

Unlike land-based explosive ordnance, fragmentation due to underwater ordnance is seldom regarded as a primary hazard for munitions found in the maritime environment (Szturomski, 2015; Nowak et al., 2024b). In most underwater UXO risk assessments for offshore infrastructure (Alpha Associates Ltd, 2011; Ordtek, 2023), the dominant threat is considered to be the underwater shock wave. However, when a cased explosive charge is positioned near the free surface, the detonation can generate high-velocity fragments capable of breaching the water column and posing a lethal risk above the water surface, as proven in this article.

This study demonstrates three principal effects associated with increasing the submersion depth of underwater ordnance explosion: 1) a reduction in the number of fragments emerging from the water; 2) a decrease in fragment velocity; and 3) an apparent increase in fragmentation size recorded in the witness panels when compared to air tests. Fewer projectiles correspondingly reduce the probability of a target being struck at a given distance. Small-scale explosive tests were conducted and the results used to directly compare fragment behaviour in air and at various submersion depths, highlighting the damping influence of water. Although limited by charge size and casing geometry, the results clearly indicate a correlation between detonation depth and the fragmentation behaviour of steel-cased munitions of larger scale.

This study introduced a predictive analysis of fragment trajectories and potential injury zones, using steel ball bearings as surrogate fragmentation mass. For each configuration, flight paths were computed under unobstructed conditions, and injury zones were determined from kinetic-energy-density criteria.

The modelling indicates that increasing submersion depth substantially reduces both maximum fragment range and the corresponding hazardous distances.

These results reinforce the conclusion that water depth is a key mitigating parameter in fragment hazard assessment. For shallow charges, fragment velocity and density remain sufficient to cause above-surface injuries, but as the depth increases, water confinement rapidly reduces both physical magnitudes. The total recovered fragment mass remains a useful indicator of casing breakup but does not fully capture the directionality or energy decay relevant to operational risk assessment.

Considering scaling differences between small-scale trials and full-scale ordnance, the findings underline the significant fragmentation risk associated with explosive remnants located in shallow water. The results hereby presented should raise awareness among EOD personnel engaged in explosive ordnance disposal that increasing detonation depth can be an effective mitigation measure. Current military procedures lack a standardised method for determining safe standoff distances as a function of depth, and this gap warrants urgent attention.

Future work will focus on validating these small-scale observations against both the existing Swisdak and Montonaro (1992) predictions and new larger scale data to fully assess and validate similitude scalability of underwater fragmentation; the results of which would refine predictive and more practical models for operational use.

5. Acknowledgements

This work has been supported by the Polish National Agency for Academic Exchange (NAWA) under the STER program, Towards Internationalization of Poznan University of Technology Doctoral School (2022-2024). A portion of the experimental work was funded by the Defence Science and Technology Laboratory (Dstl). Additionally, the assistance of the University of Sheffield technical staff at the Buxton Blast laboratory in preparing the facility and conducting the experimental work is gratefully acknowledged.

6. References

Absil LHJ, Kodde HH, Weerheijm J (1996) Evaluation of Safety Distances for UXO Disposal Operations. TNO Prins Maurits Laboratory, Research Group Explosion Prevention and Protection.

Alpha Associates Ltd (2011) Unexploded Ordnance (UXO) Threat & Risk Assessment with Risk Mitigation Strategy. Aberdeen Offshore Wind Farm.

Australian Munitions (2016) Hand grenades – Designed for operational effectiveness.

Charron YJ (1979) Estimation of velocity distribution of fragmenting warheads using a modified Gurney method. Air Force Institute of Technology, Air Training Command.

Cooper PW (1997) Explosive engineering. Wiley-VCH. ISBN 0-471-18636-8.

Department of the Army (1973) Ammunition and Explosives Standards, TM 9-1300-206.

Department of the Army (2011) Safety Ammunition and Explosives Safety Standards, Pamphlet 385–64.

Department of the Army (2013) Explosive Ordnance Disposal (EOD) operations, ATP 4-32.

Departments of the Army, Navy and Air Force (1990) Structures to resist the effects of accidental explosions, Army TM 5-1300.

Diehl Defence (2010) Hand Grenades, Hand Grenade Fuzes.

Farrimond D, Ratcliff A, Dennis A, Rigby SE, Tyas A, Clarke SD, Lodge TL, Tolman W (2023) MicroBlast – a benchmarking study of gramme-scale explosive trials. In: Proceedings of the 26th International Symposium on Military Aspects of Blast and Shock (MABS26), Australia.

Farrimond DG, Rigby SE, Clarke SD, Tyas A (2022) Time of arrival as a diagnostic for far-field high explosive blast waves. Int J Protective Structures 13(2):379–402. doi:10.1177/20414196211062923.

Farrimond DG, Woolford S, Tyas A, et al (2024) Far-field positive phase blast parameter characterisation of RDX and PETN based explosives. Int J Protective Structures 15(1):141–165. doi:10.1177/20414196221149752.

Fan Y, Chen L, Xiang HB, Fang Q, Han FY (2023) Lead spall velocity of fragments of ultra-high-performance concrete slabs under partially embedded cylindrical charge-induced explosion. Defence Technology. https://doi.org/10.1016/j.dt.2022.02.009.

Foley S, Sherman D, Davis A, MacDonald R, Bir C (2023) Evaluation of Skin Penetration from Less Lethal Impact Munitions and Their Associated Risk Predictors. SAE Int J Transportation Safety.

Frem D (2023) A mathematical model for estimating the Gurney velocity of chemical high explosives. FirePhysChem. https://doi.org/10.1016/j.fpc.2022.11.002.

Gebbeken N, Rüdiger L, Warnstedt P (2019) Explosion mitigation by water mist-ring mesh with water curtain. Proc 25th Military Aspects of Blast and Shock Conf, The Hague.

Geneva International Centre for Humanitarian Demining – GICHD (2015) A guide to survey and clearance of Underwater Explosive Ordnance.

Geneva International Centre for Humanitarian Demining – GICHD (2017) Explosive weapon effects – final report. Geneva. ISBN 978-2-940369-61-4.

Geneva International Centre for Humanitarian Demining – GICHD (2022) Explosive Ordnance Guide for Ukraine.

Gurney RW (1943) The Initial Velocities of Fragments from Bombs, Shells, and Grenades. Ballistic Research Laboratory Report BRL-405, Aberdeen, Maryland.

HELCOM – Helsinki Commission (2024) Thematic assessment on Hazardous Submerged Objects in the Baltic Sea. Submerged Assessment – Warfare Materials in the Baltic Sea.

Landau LD, Lifshitz EM (1987) Fluid Mechanics: Course of Theoretical Physics. 2nd edition.

Lee JJ, Rude G (2006) Underwater fragmentation of cylinders. Defence R&D Canada.

Li X, Dong J, Wang W, Liang Z (2024) Modification of axial distribution of fragment velocity in preformed fragmentation warheads. Central European J Energetic Materials 21(1):22–52. doi:10.22211/cejem/186374.

McCleskey F, Neades DN, Rudolph RR (1990) A Comparison of Two Personnel Injury Criteria Based on Fragmentation. Proc 24th DoD Explosives Safety Seminar, Aug. 1990.

McMahon GE (1971) The relationship between velocity of impact and penetration into strawboard of fragments of different densities. RARDE, 26 Nov 1971.

Montanaro PE (1990) TRAJ – A Two-Dimensional Trajectory Program For Personal Computers. Proc 24th DoD Explosives Safety Seminar.

Morrison FA (2016) Data Correlation for Drag Coefficient for Sphere. Michigan Technological University.

Nowak PR (2021) Neutralizacja historycznego uzbrojenia wojskowego o dużym wagoniarze materiału wybuchowego w ramach oczyszczania akwenów z przedmiotów wybuchowych i niebezpiecznych. Rocznik Bezpieczeństwa Morskiego. ISSN 1898-3189.

Nowak PR, Jodlowski M, Sielicki PW (2021) “Tallboy” bomb neutralization – New technologies in UXO disposal in the marine environment. NATO EOD Centre of Excellence. ISBN 978-80-89261-93-2.

Nowak PR, Gajewski T, Szlachta A, Sielicki PW (2024b) Explosive Materials Management Near Maritime Critical Infrastructure – Safe Disposal Considerations. NATO Science for Peace and Security, vol. 65. doi:10.3233/NICSP240019.

Nowak PR, Waddoups R., Farrimond D. G., Gajewski T., Lodge T., Langdon G., Tyas A., Sielicki P., Tam E & Whittaker M. (2024a). A fragmentation assessment method for submerged charges. In Proceedings of the 19th ISIEMS. International Symposium on Interaction of the Effects of Munitions with Structures (ISIEMS).

Ordtek Ltd (2023) Unexploded Ordnance (UXO) Risk Management – Potential UXO Predictive Numbers. Dogger Bank South Offshore Wind Farm Report.

Rohne H (1906) Schiesslehre für Infanterie.

Salter SH, Parkes JH (1994) The use of water-filled bags to reduce the effects of explosives. The University of Edinburgh.

Schunck T, Eckenfels D (2021) Experimental study of explosion mitigation by deployed metal combined with water curtain. Appl Sci 11:6539. doi:10.3390/app11146539.

Schunck T, Eckenfels D (2024) Explosion mitigation by grids in combination with a water curtain. Int J Protective Structures. doi:10.1177/20414196241271454.

Sielicki PW, Stewart MG, Gajewski T, Malendowski M, Peksa P, Al-Rifaie H, Studziński R, Sumelka W (2021) Field test and probabilistic analysis of irregular steel debris casualty risks from a person-borne improvised explosive device. Defence Technology. https://doi.org/10.1016/j.dt.2020.10.009.

Solomos G, Larcher M, Valsamos G, Karlos V, Casadei F (2020) A survey of computational models for blast induced human injuries for security and defence applications. JRC Technical Reports, European Commission, Ispra, Italy. ISBN 978-92-76-14659-9. doi:10.2760/685.

Swisdak MM, Montanaro PE (1992) Hazards from Underwater Explosions. Naval Surface Warfare Center.

Szturomski B (2015) The effect of an underwater explosion on a ship. Zeszyty Naukowe Akademii Marynarki Wojennej 201:57–73. doi:10.5604/0860889X.1172074.

United Nations (2013) International Mine Action Standard (IMAS 10.20): Safety & occupational health – Demining worksite safety.

United Nations (2021) International Ammunition Technical Guidelines (IATG 10.10): Demilitarization, destruction and logistic disposal of conventional ammunition.

United Nations (2021) International Mine Action Standard (IMAS 09.60): Underwater survey and clearance of explosive ordnance (EO).

United Nations Office for Disarmament Affairs – UNODA (2021) International Ammunition Technical Guidelines 01.80: Formulae for ammunition management.

Whiting A (2011) Report on work carried to establish airsoft threshold lethality. Forensic Science Service, Southern Firearms Unit London, Lab Ref 300974287.

Zaker TA (1975) Fragment and Debris Hazards. Department of Defense Explosives Safety Board Technical Paper 12.

Zecevic B, Catovic A, Terzic J (2008) Comparison of lethal zone characteristics of several natural fragmenting warheads. Central European J Energetic Materials 5(2):67–81.

Zhao Ch, Wang S, Guo C, Liu D, Ma F (2020) Experimental study on fragmentation of explosive loaded steel projectile. Int J Impact Eng 144:103610. doi:10.1016/j.ijimpeng.2020.103610.

Appendix A

This appendix presents the results obtained from the 20-layer witness panels used during the fragmentation tests. The table below summarises the total number of fragment impacts recorded on the panels and the number of layers perforated for each test shot.

Fragment Impact and Penetration – all shots.

	Type of casing	Test setup	Number of perforated layers	Fragments number
1	Machined	(A) air	13	180
2			11	199
3	1.7 mm ball	(A) air	9	281
4			9	290
5	Machined	(B) half-submerged	14	157
6			11	197
7			12	140
8	1.7 mm ball	(B) half-submerged	9	298
9			9	346
10	2.6 mm ball	(B) half-submerged	10	233
11	Machined	(C) charge top at surface	13	114
12			15	120
13			14	137
14	1.7 mm ball	(C) charge top at surface	6	305
15			8	311
15			7	302
17	Machined	(D) 60 mm depth	4	8
18			7	13
19	1.7 mm ball	(D) 60 mm depth	4	327
20			3	311
21	2.6 mm ball	(D) 60 mm depth	3	162
22			4	165
23			4*	265*
24	Machined	(E) 110 mm depth	0	0
25			0	0
26			1	3
27	1.7 mm ball	(E) 110 mm depth	1	4
28			0	0
29	2.6 mm ball	(E) 110 mm depth	1	105
30			1	127

* The witness panel in this shot was rotated 90° to verify the fragment capture efficiency under altered panel orientation.

Appendix B

This appendix presents the fragment density in the first witness panel for the three types of casing material and with the maximum number of fragments recovered in each test setup.

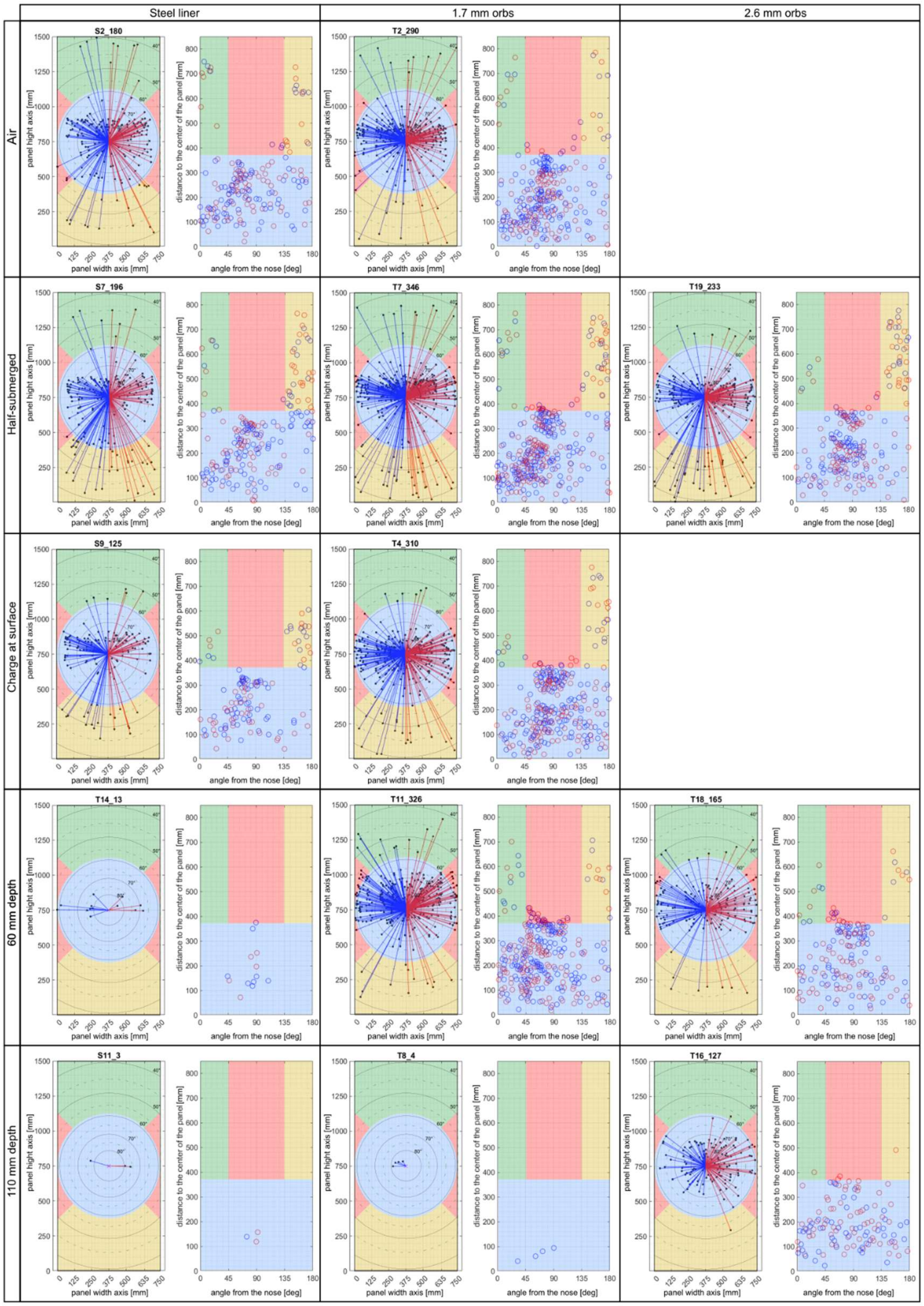

Appendix C

Calculated fragmentation patterns for 1.7 mm and 2.6 mm balls for all the tests.

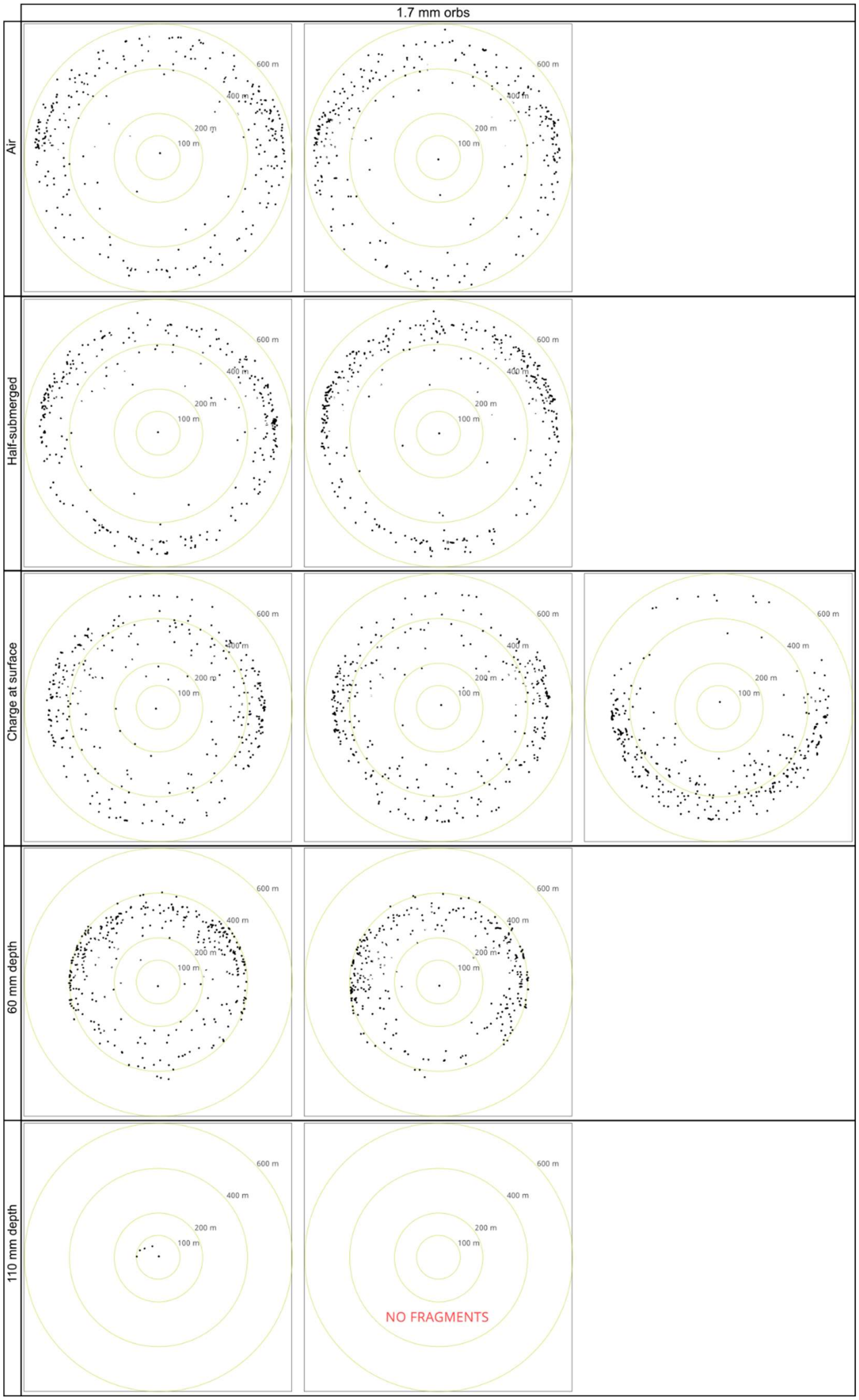

	2.6 mm orbs		
Air			
Half-submerged	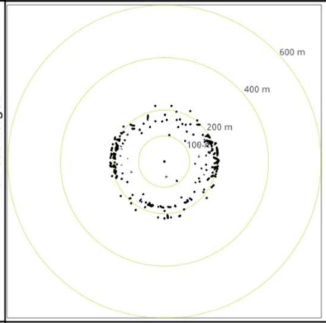		
Charge at surface	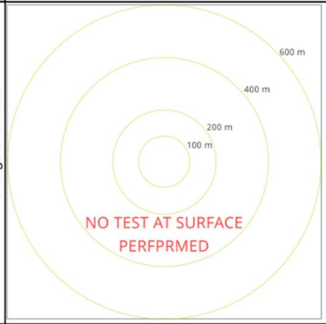		
60 mm depth	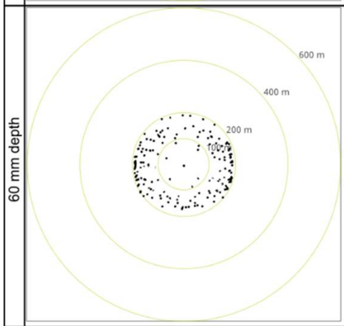	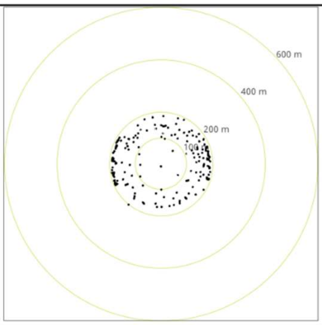	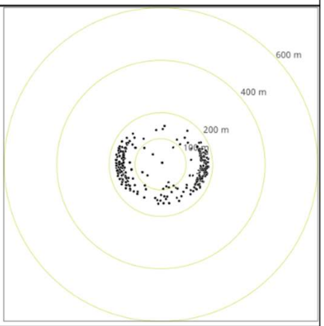
110 mm depth